

## COMMUNICATION



Cite this: *Sustainable Energy Fuels*,  
2020, 4, 5498

Received 22nd July 2020  
Accepted 11th September 2020

DOI: 10.1039/d0se01088j

rsc.li/sustainable-energy

# Iron nanoparticles loaded on nickel sulfide nanosheets: an efficient amorphous catalyst for water oxidation†

Changtong Lu,<sup>a</sup> XianKang Niu,<sup>a</sup> WenHui Zhang,<sup>a</sup> Fengli Qu <sup>\*a</sup> and Limin Lu <sup>\*b</sup>

Although recent studies on the oxygen evolution reaction (OER) have achieved great progress, it remains a great challenge to achieve a smaller overpotential at high current density. In order to further improve the performance of the OER, we adopted a novel method to load Fe nanoparticles on a Ni<sub>3</sub>S<sub>2</sub> nanoplate array grown on nickel foam (Fe NPs-Ni<sub>3</sub>S<sub>2</sub> NA/NF) which formed an amorphous structure. In particular, this catalyst exhibited an overpotential of 206 mV at 150 mA cm<sup>-2</sup>, outmatching most non-noble OER catalysts reported so far; it also operates smoothly in various stability tests.

## Introduction

Hydrogen fuel, as a clean-energy resource with zero greenhouse gas emissions and high energy density, is widely regarded as a promising alternative to traditional fossil fuels.<sup>1-4</sup> Electrochemical water splitting is one of the most efficient, sustainable, economic and non-polluting approaches to produce hydrogen energy.<sup>5-7</sup> Unfortunately, the oxygen evolution reaction (OER) is the rate-determining step due to its slow kinetics.<sup>8-10</sup> Over the past decade, the most active state-of-the-art OER catalysts have been compounds containing noble metals (such as IrO<sub>2</sub> and RuO<sub>2</sub>). However, their application has been hindered because of their high cost and relative scarcity.<sup>11-13</sup> Therefore, exploring low-cost and ultra-efficient OER electrocatalysts is critical for future development.<sup>14-18</sup>

At present, NiS<sub>x</sub> (e.g., NiS, NiS<sub>2</sub>, and Ni<sub>3</sub>S<sub>2</sub>) have attracted much attention due to their intrinsic metallic behaviors with high conductivity.<sup>19-25</sup> But NiS<sub>x</sub> exhibit poor performance in terms of bad stability and high overpotential ( $\eta$ ) for water

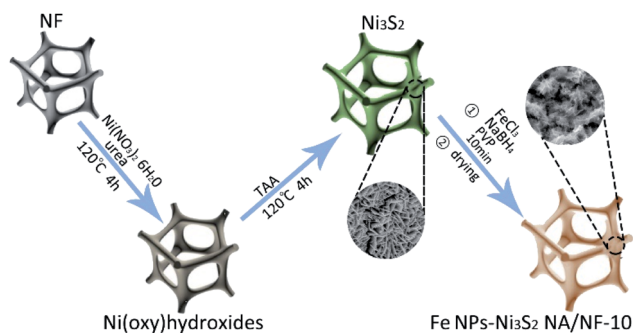
splitting under alkaline conditions.<sup>26,27</sup> Typically, the doping of metal elements and the construction of heterostructures are considered to be the two most effective strategies for improving the catalytic performance.<sup>15,28,29</sup> However, the optimized catalytic performance still cannot meet the actual production needs of enterprises. In order to further improve the activity of the catalyst, the construction of an amorphous Ni-based catalyst by introducing foreign elements has attracted our attention. The incorporation of foreign elements will lead to a relatively disordered structure, which has a larger surface area and lower steric hindrance for the adsorption and desorption of hydrogen/oxygen-containing substances.<sup>30-32</sup> Moreover, the amorphous structure formed by the introduction of foreign elements has the inherent structural characteristics of long-range disorder and short-range order and has abundant defects and active sites.<sup>33-35</sup> In recent years, catalysts containing nickel and iron have exhibited excellent oxygen evolution reaction performance.<sup>36-40</sup> Although the function of iron (Fe) is still controversial, the presence of Fe is very important for high activity.<sup>41</sup> Studies have shown that the presence of Fe can lead to amorphous characteristics.<sup>42,43</sup> The loading of an appropriate number of Fe nanoparticles can optimize the local electronic configuration of the Ni-based active center, thereby making the catalyst more reactive.<sup>44,45</sup> Therefore, we speculate that loading Fe nanoparticles on NiS<sub>x</sub> will greatly improve the performance of the OER, but no catalysts have been reported.

In this work, Fe nanoparticles loaded on a Ni<sub>3</sub>S<sub>2</sub> nanoplate array grown on nickel foam (Fe NPs-Ni<sub>3</sub>S<sub>2</sub> NA/NF) was successfully synthesized *via* a three-step procedure including a two-step thermal process and a one-step NaBH<sub>4</sub> reduction (Scheme 1). In order to prevent Fe nanoparticles from being oxidized by air, reduction of Fe(III) ions was carried out in a nitrogen atmosphere. We successively adjusted the reduction time of trivalent iron to 5, 10, 15 and 20 minutes, and the resultant products were referred to as Fe NPs-Ni<sub>3</sub>S<sub>2</sub> NA/NF-5, Fe NPs-Ni<sub>3</sub>S<sub>2</sub> NA/NF-10, Fe NPs-Ni<sub>3</sub>S<sub>2</sub> NA/NF-15 and Fe NPs-Ni<sub>3</sub>S<sub>2</sub> NA/NF-20, respectively. Fe NPs-Ni<sub>3</sub>S<sub>2</sub> NA/NF-10 exhibits excellent OER performance and it only requires 206 mV to drive 150 mA cm<sup>-2</sup>

<sup>a</sup>College of Chemistry and Chemical Engineering, Qufu Normal University, Qufu, Shandong 273165, P. R. China. E-mail: fengliqun@hotmail.com

<sup>b</sup>Institute of Functional Materials and Agricultural Applied Chemistry, College of Science, Jiangxi Agricultural University, Nanchang 330045, P. R. China. E-mail: lulimin816@hotmail.com

† Electronic supplementary information (ESI) available: Experimental section and supplementary figures. See DOI: 10.1039/d0se01088j



Scheme 1 Schematic illustration of the synthesis process for the Fe NPs- $\text{Ni}_3\text{S}_2$  NA/NF.

for the OER. In addition, Fe NPs- $\text{Ni}_3\text{S}_2$  NA/NF-10 presents good long-term electrochemical durability with the maintenance of its catalytic activity for at least 30 h at a current density of  $80 \text{ mA cm}^{-2}$ . In addition, this catalyst achieves a high turnover frequency (TOF) of  $0.123 \text{ mol O}_2 \text{ s}^{-1}$  at an overpotential of 300 mV.

## Results and discussion

The structure and morphology of the as-prepared  $\text{Ni}_3\text{S}_2$  nanosheet array on Ni foam ( $\text{Ni}_3\text{S}_2$  NA/NF) and Fe NPs- $\text{Ni}_3\text{S}_2$  NA/NF-10 nanosheets can be observed by scanning electron

microscopy (SEM) and transmission electron microscopy (TEM), respectively. Fig. 1a and c show that the prepared  $\text{Ni}_3\text{S}_2$ /NF with fewer pores has a sheet-like shape where the nanosheets are unavoidably stacked together, hindering the contact with the electrolyte. In comparison, Fe NPs- $\text{Ni}_3\text{S}_2$  NA/NF-10 newly forms a large number of wrinkled nanosheets with a smaller size in the nanoscale range, where the surface is rougher and the pores are more numerous (Fig. 1b and d). Therefore, in the process of loading Fe nanoparticles on  $\text{Ni}_3\text{S}_2$  NA/NF, the stacked large sheets are broken into relatively dispersed small sheets, which increases the surface area and greatly increases the number of active sites. In addition, Fig. S1† displays the SEM image of Fe NPs- $\text{Ni}_3\text{S}_2$  NA/NF-10, suggesting that numerous nanoparticles are present in the structure. The energy-dispersive X-ray (EDX) elemental mapping images of Fe NPs- $\text{Ni}_3\text{S}_2$  NA/NF-10 verify the uniform distribution of Ni, Fe and S elements (Fig. S2†). In addition, to eliminate the interference of Ni foam, we also measured the element content (Fig. S3†). The mass ratio of Fe : Ni is confirmed by inductively coupled plasma mass spectrometry (ICP-MS). The atomic ratio of Ni : Fe is identified to be around 8 : 1 (Table S1†). The high-resolution transmission electron microscopy (HRTEM) image in Fig. 1e confirms the formation of  $\text{Ni}_3\text{S}_2$  nanosheets with obvious crystalline character. The lattice fringe spacing of 0.28 and 0.23 nm can be ascribed to the (110) and (003) planes of  $\text{Ni}_3\text{S}_2$  (JCPDS no. 76-1870). After Fe nanoparticles were introduced, Fe NPs- $\text{Ni}_3\text{S}_2$  NA/NF-10 became an amorphous structure, the long-range atomic arrangement was disrupted, and the quantity of defect sites increased (Fig. 1f). The SAED pattern of  $\text{Ni}_3\text{S}_2$  NA/NF (Fig. S4a†) shows diffraction spots, which suggests a crystalline nature. In contrast, the SAED pattern of Fe NPs- $\text{Ni}_3\text{S}_2$  NA/NF-10 (Fig. S4b†) suggests weak crystallinity. We attribute this to the Fe induced structural disorder of the active nickel site. These results indicate that  $\text{Ni}_3\text{S}_2$  retained its crystal structure and the Fe NPs- $\text{Ni}_3\text{S}_2$  NA/NF-10 had an amorphous structure.

The X-ray diffraction (XRD) patterns further verify the amorphous nature of the Fe NPs- $\text{Ni}_3\text{S}_2$  NA/NF-10. Fig. 2a presents the X-ray diffraction (XRD) patterns for  $\text{Ni}_3\text{S}_2$  NA/NF and Fe NPs- $\text{Ni}_3\text{S}_2$  NA/NF-10.  $\text{Ni}_3\text{S}_2$  NA/NF displayed strong diffraction peaks at around  $21.76^\circ$ ,  $31.13^\circ$ ,  $37.78^\circ$ ,  $50.16^\circ$  and  $55.19^\circ$  which were indexed to the (101), (110), (003), (211) and (122) planes of  $\text{Ni}_3\text{S}_2$  (JCPDS no. 76-1870), respectively. Three other peaks were observed at  $44.50^\circ$ ,  $51.80^\circ$  and  $76.40^\circ$  due to the presence of nickel foam (JCPDS no. 04-0850). It is worth noting that as the loading of Fe nanoparticles increases, the diffraction peaks of  $\text{Ni}_3\text{S}_2$  show different degrees of broadening instead of shifting (Fig. S5†). This indicates that the loading of Fe nanoparticles has a great influence on the crystal structure of  $\text{Ni}_3\text{S}_2$ , leading to the distortion of the crystal grains and the increase of lattice defects, resulting in grain distortion and increased lattice defects. This phenomenon is also consistent with the conclusions drawn by HRTEM. The X-ray photoelectron spectroscopy (XPS) survey spectrum further confirmed the presence of Ni, Fe and S elements (Fig. S6†). The high-resolution Ni 2p spectrum is shown in Fig. 3b. The spectrum of  $\text{Ni}_3\text{S}_2$  NA/NF shows binding energies (BEs) corresponding to Ni 2p<sub>3/2</sub> and Ni 2p<sub>1/2</sub> positioned at 856.0 and 873.7 eV, respectively, which confirm the presence

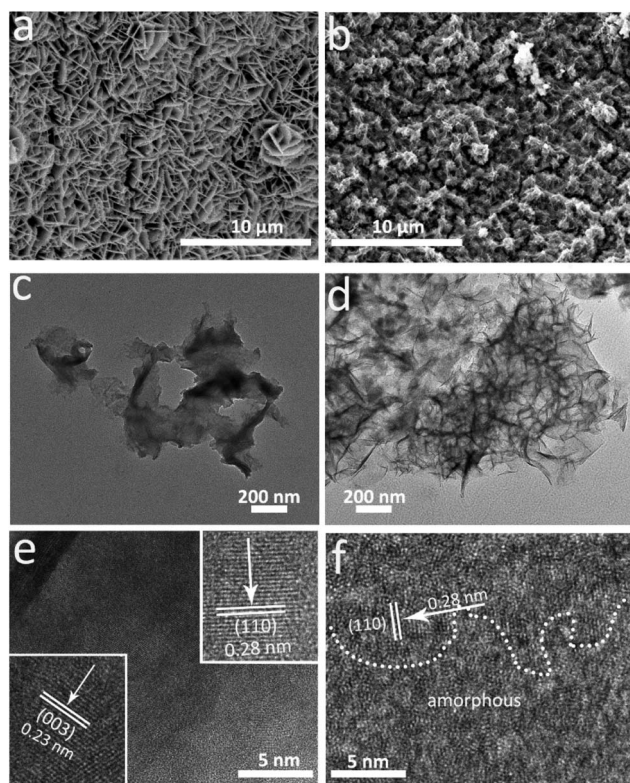


Fig. 1 SEM image of (a)  $\text{Ni}_3\text{S}_2$  NA/NF and (b) Fe NPs- $\text{Ni}_3\text{S}_2$  NA/NF-10. TEM image of (c)  $\text{Ni}_3\text{S}_2$  and (d) Fe NPs- $\text{Ni}_3\text{S}_2$  NA/NF-10. HRTEM image of (e)  $\text{Ni}_3\text{S}_2$  nanosheets and (f) Fe NPs- $\text{Ni}_3\text{S}_2$  NA/NF-10 nanosheets.

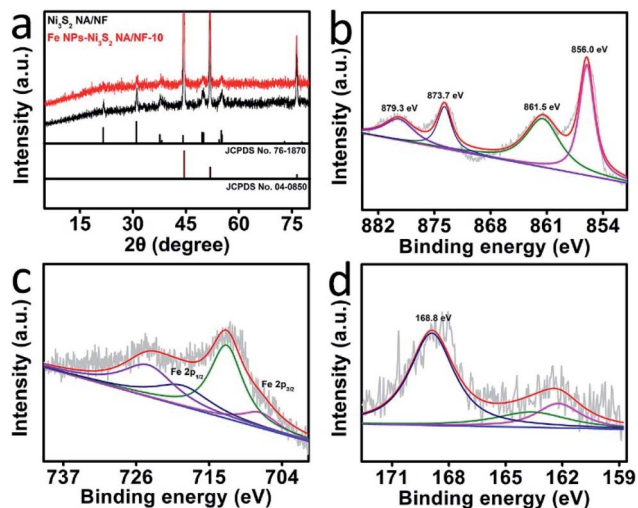


Fig. 2 (a) XRD patterns of  $\text{Ni}_3\text{S}_2$  NA/NF and Fe NPs- $\text{Ni}_3\text{S}_2$  NA/NF-10. XPS spectra in the (b) Ni 2p, (c) Fe 2p and (d) S 1s regions for Fe NPs- $\text{Ni}_3\text{S}_2$  NA/NF-10.

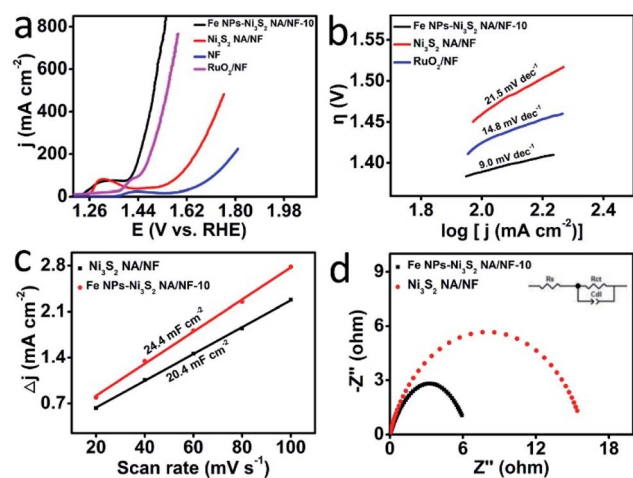


Fig. 3 (a) Linear sweep voltammetry OER curves. (b) Tafel plots of  $\text{RuO}_2/\text{NF}$ ,  $\text{Ni}_3\text{S}_2$  NA/NF and Fe NPs- $\text{Ni}_3\text{S}_2$  NA/NF-10. (c) Double-layer capacitance determined by the current density at different scan rates. (d) Electrochemical impedance spectroscopy (EIS) Nyquist plots.

of  $\text{Ni}^{2+}$ .<sup>5,46</sup> Interestingly, compared with the Ni 2p<sub>3/2</sub> peak of  $\text{Ni}_3\text{S}_2$  NA/NF and Fe NPs- $\text{Ni}_3\text{S}_2$  NA/NF-10, the peak positions of Fe NPs- $\text{Ni}_3\text{S}_2$  NA/NF-10 shift to higher binding energies (Fig. S7†). This suggests that a synergistic effect between two metals occurs when Fe NPs- $\text{Ni}_3\text{S}_2$  NA/NF-10 is formed, which is not a simple physical adsorption. Fig. 2c shows that the XPS spectrum of Fe 2p exhibits two chemically different species, including metallic Fe (707.3 eV and 719.0 eV) and the oxidation state of Fe species (712.3 eV and 724.3 eV).<sup>47</sup> The oxide species of Fe indicate that the surface of Fe NPs- $\text{Ni}_3\text{S}_2$  NA/NF-10 is partially oxidized or interacts with the adsorbed  $\text{O}_2$ . In Fig. 2d, the peak at 162.2 eV is attributed to  $\text{S}^{2-}$ , while the one at 163.4 eV comes from the sulfur substance, which is usually the reaction product of thioacetamide.<sup>48,49</sup>

The electrochemical performances of Fe NPs- $\text{Ni}_3\text{S}_2$  NA/NF-10 were analyzed *via* the linear sweep voltammetry (LSV) technique using a typical three electrode system with a scan rate of  $5 \text{ mV s}^{-1}$  in  $1.0 \text{ M KOH}$ . For comparison, the electrocatalytic activity of  $\text{Ni}_3\text{S}_2$  NA/NF, nickel foam (NF), and commercial  $\text{RuO}_2$  on nickel foam ( $\text{RuO}_2/\text{NF}$ ) was tested under the same conditions. To reflect the intrinsic behavior of the catalysts, all experimental data were corrected with ohmic potential drop ( $iR$ ) losses resulting from the solution resistance. In Fig. 3a, the oxidation peak at a lower potential (1.25 to 1.40 V vs. RHE) corresponds to the transition from  $\text{Ni}^{2+}$  to  $\text{Ni}^{3+}$ . The introduction of an appropriate amount of Fe will inhibit the oxidation of  $\text{Ni}^{2+}$ .<sup>50,51</sup> This is also the reason why the oxidation peak of Fe NPs- $\text{Ni}_3\text{S}_2$  NA/NF-10 is lower than that of  $\text{Ni}_3\text{S}_2/\text{NF}$  at lower overpotential (1.25 to 1.40 V vs. RHE). The Fe NPs- $\text{Ni}_3\text{S}_2$  NA/NF-10 exhibits an overpotential of 206 mV at a current density of  $150 \text{ mA cm}^{-2}$ , which is obviously smaller than those of  $\text{Ni}_3\text{S}_2/\text{NF}$  (391 mV) and commercial  $\text{RuO}_2/\text{NF}$  (240 mV). Fe NPs- $\text{Ni}_3\text{S}_2$  NA/NF-10 also exhibits a superb catalytic performance compared with other similar catalysts (Table S2†). In order to avoid the influence of different scanning speeds on the catalytic performance, LSV with a scanning speed of  $1 \text{ mV s}^{-1}$  was performed to prove the stability of the material at different scanning speeds (Fig. S8a†). The catalytic performances in 30 wt% KOH and 0.1 M KOH were further tested. Fe NPs- $\text{Ni}_3\text{S}_2$  NA/NF-10 needs an overpotential of 139 mV and 440 mV in 30 wt% KOH and 0.1 M KOH, respectively, to drive a current density of  $150 \text{ mA cm}^{-2}$ , as shown in the result (Fig. S8b†). The Tafel slope evolving from the LSV curve is essential for evaluating the dynamic characteristics of the OER. As expected, the lower Tafel slope of Fe NPs- $\text{Ni}_3\text{S}_2$  NA/NF-15 ( $9.0 \text{ mV dec}^{-1}$ ) is also lower than those of  $\text{Ni}_3\text{S}_2/\text{NF}$  ( $21.5 \text{ mV dec}^{-1}$ ) and commercial  $\text{RuO}_2/\text{NF}$  ( $14.8 \text{ mV dec}^{-1}$ ), implying superior OER catalytic kinetics on Fe NPs- $\text{Ni}_3\text{S}_2$  NA/NF-10 (Fig. 3b). The duration of  $\text{NaBH}_4$  reduction will affect the iron content in the catalyst; therefore, the OER performance of the catalyst will also be affected. And overpotentials of 240, 230 and 250 mV were needed to afford  $150 \text{ mA cm}^{-2}$  (Fig. S9a†) along with larger Tafel slopes of 11.9, 12.4 and  $10.3 \text{ mV dec}^{-1}$  (Fig. S9b†) for Fe NPs- $\text{Ni}_3\text{S}_2$  NA/NF-5, Fe NPs- $\text{Ni}_3\text{S}_2$  NA/NF-15 and Fe NPs- $\text{Ni}_3\text{S}_2$  NA/NF-20, respectively.

In addition, to better understand the catalytic activity, the electrochemically active surface area (ECSA) was estimated from the double-layer capacitance ( $C_{\text{dl}}$ ).<sup>52,53</sup> Specifically, the  $C_{\text{dl}}$  was obtained using the equation  $i = \nu C_{\text{dl}}$  where  $i$  denotes the cathodic charging current in CV obtained with different scan rates  $\nu$  in a non-faradaic region (Fig. S10†).<sup>54</sup> As observed in Fig. 3c, Fe NPs- $\text{Ni}_3\text{S}_2$  NA/NF-10 demonstrates a higher  $C_{\text{dl}}$  than  $\text{Ni}_3\text{S}_2$  NA/NF. As we all know, the ECSA is positively correlated with the  $C_{\text{dl}}$  of the catalyst.<sup>55</sup> Then the ECSA was estimated from the equation  $\text{ECSA} = C_{\text{dl}}/C_s$  where  $C_s$  is the specific capacitance ( $0.04 \text{ mF cm}^{-2}$ ).<sup>56,57</sup> The ECSA value of Fe NPs- $\text{Ni}_3\text{S}_2$  NA/NF-10 ( $610 \text{ cm}^{-2}$ ) is better than that of  $\text{Ni}_3\text{S}_2$  NA/NF ( $510 \text{ cm}^{-2}$ ), indicating that Fe nanoparticle loading effectively improves the roughness of  $\text{Ni}_3\text{S}_2$  NA/NF nanosheets and is beneficial for exposing more active sites. Electrochemical impedance spectroscopy (EIS) tests also uncovered that the appropriate contents of Fe introduced can increase electrical conductivity

and enhance the catalytic performance (Fig. 3d). The best way to compare the intrinsic activity of catalyst materials is through their turnover frequency (TOF), that is, the number of O<sub>2</sub> molecules evolved per second per active site.<sup>13,57</sup> As presented in Fig. S11,† the TOF value (0.123 O<sub>2</sub> s<sup>-1</sup> η = 300 mV) of Fe NPs-Ni<sub>3</sub>S<sub>2</sub> NA/NF-10 is also higher than that of Ni<sub>3</sub>S<sub>2</sub> NA/NF (0.03 O<sub>2</sub> s<sup>-1</sup> η = 300 mV), implying superior OER catalytic kinetics on Fe NPs-Ni<sub>3</sub>S<sub>2</sub> NA/NF-10. The TOF value of Fe NPs-Ni<sub>3</sub>S<sub>2</sub> NA/NF-10 is superior to those of most reported OER catalysts (Table S3†).

Stability is a key factor to measure whether the catalyst with excellent performance can be used in actual production.<sup>25,58</sup> The LSV curve of Fe NPs-Ni<sub>3</sub>S<sub>2</sub> NA/NF-10 after 1000 cycles shows a negligible decline, demonstrating excellent catalytic stability (Fig. 4a). It was proved that the material after 1000 cycles still maintained the same content ratio of Ni : Fe obtained by ICP-MS (Table S1†), the characteristics of sulfide and the nano-sheet structure as observed through the XRD (Fig. S12a†), SEM (Fig. S12b†) and TEM (Fig. S12c†) compared with the original materials, which demonstrated the stability of the material. Besides, Fe NPs-Ni<sub>3</sub>S<sub>2</sub> NA/NF-10 is demonstrated to have excellent mass transport properties (inset in Fig. 4a). In addition, the long-term stability of the Fe NPs-Ni<sub>3</sub>S<sub>2</sub> NA/NF-10 toward the OER was estimated by chronopotentiometry measurements. As shown in Fig. 4b, the constant current density of 80 mA cm<sup>-2</sup> remains unchanged under the operating conditions for 30 h, proving the satisfactory stability. The faradaic efficiency of this electrode for the OER was determined to be 100% (Fig. S13†), implying that the current density is proportional to oxygen generation.<sup>59,60</sup>

In summary, a series of amorphous Fe NPs-Ni<sub>3</sub>S<sub>2</sub> NA/NF fabricated with different contents of Fe have been successfully synthesized and further investigated as catalysts for the OER. The optimized catalyst Fe NPs-Ni<sub>3</sub>S<sub>2</sub> NA/NF-10 exhibits a lower overpotential (206 mV at a current density of 150 mA cm<sup>-2</sup>) and excellent long-term stability (strong current density for 30 h without fading). Besides, this catalyst achieves a high turnover frequency (TOF) of 0.123 mol O<sub>2</sub> s<sup>-1</sup> at an overpotential of 300 mV. The performance of Fe NPs-Ni<sub>3</sub>S<sub>2</sub> NA/NF-10 is better than that of almost all non-noble metal OER electrocatalysts so far. This work helps us to further improve the performance of

OER catalysts and may provide a universal route towards design and fabrication of ultra-low overpotential OER electrocatalysts.

## Conflicts of interest

There are no conflicts to declare.

## Acknowledgements

This work was supported by the National Natural Science Foundation of China (21775089, 51862014, and 21665010), Outstanding Youth Foundation of Shandong Province (ZR2017JL010), Taishan scholar of Shandong Province (tsqn201909106) and Key Research and Development Program of Jining City (2018ZDGH032).

## References

- H. Du, R. Kong, X. Guo, F. Qu and J. Li, *Nanoscale*, 2018, **10**, 21617–21624.
- C. Wu, Y. Yang, D. Dong, Y. Zhang and J. Li, *Small*, 2017, **13**, 1602873.
- J. Tian, Q. Liu, A. Asiri and X. Sun, *J. Am. Chem. Soc.*, 2014, **136**, 7587–7590.
- X. Luan, H. Du, Y. Kong, F. Qu and L. Lu, *Chem. Commun.*, 2019, **55**, 7335–7338.
- X. Guo, R. Kong, X. Zhang, H. Du and F. Qu, *ACS Catal.*, 2018, **8**, 651–655.
- S. Li, G. Zhang, X. Tu and J. Li, *ChemElectroChem*, 2018, **5**, 701–707.
- Z. W. Seh, J. Kibsgaard, C. F. Dickens, I. Chorkendorff, J. K. Nørskov and T. F. Jaramillo, *Science*, 2017, **355**, eaad4998.
- M. Sun, D. Davenport, H. Liu, J. Qu, M. Elimelech and J. Li, *J. Mater. Chem. A*, 2018, **6**, 2527–2539.
- T. Y. Ma, S. Dai, M. Jaroniec and S. Z. Qiao, *J. Am. Chem. Soc.*, 2014, **136**, 13925–13931.
- W. Zhu, Z. Yue, W. Zhang, N. Hu, Z. Luo, M. Ren, Z. Xu, Z. Wei, Y. Suo and J. Wang, *J. Mater. Chem. A*, 2018, **6**, 4346–4353.
- Y. Lee, J. Suntivich, K. J. May, E. E. Perry and Y. Shao-Horn, *J. Phys. Chem. Lett.*, 2012, **3**, 399–404.
- S. Dou, L. Tao, J. Huo, S. Wang and L. Dai, *Energy Environ. Sci.*, 2016, **9**, 1320.
- X. Zhang, C. Si, X. Guo, R. Kong and F. Qu, *J. Mater. Chem. A*, 2017, **5**, 17211–17215.
- X. Du, G. Ma and X. Zhang, *ACS Sustainable Chem. Eng.*, 2019, **7**, 19257–19267.
- X. Du, H. Su and X. Zhang, *ACS Sustainable Chem. Eng.*, 2019, **7**, 16917–16926.
- X. Du, H. Su and X. Zhang, *J. Catal.*, 2020, **383**, 103–116.
- C. Tang, N. Cheng, Z. Pu, W. Xing and X. Sun, *Angew. Chem., Int. Ed.*, 2015, **5**, 9351–9355.
- C. C. Mccrory, S. Jung, J. C. Peters and T. F. Jaramillo, *J. Am. Chem. Soc.*, 2013, **135**, 16977–16987.
- X. Du, W. Lian and X. Zhang, *Int. J. Hydrogen Energy*, 2018, **43**, 20627.

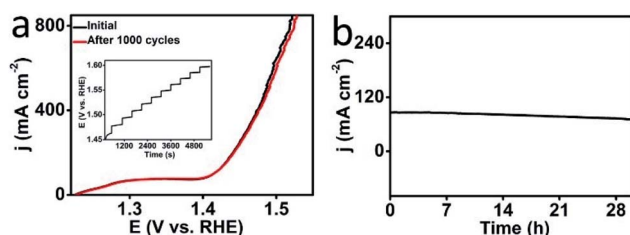


Fig. 4 (a) Polarization curves for Fe NPs-Ni<sub>3</sub>S<sub>2</sub> NA/NF-10 before and after 1000 cycles (the inset shows the multi-step chronopotentiometric curve of Fe NPs-Ni<sub>3</sub>S<sub>2</sub> NA/NF-10. The current density started at 80 mA cm<sup>-2</sup> and ended at 280 mA cm<sup>-2</sup>, with an increment of 20 mA cm<sup>-2</sup> after every 500 s). (b) Long-term stability test results of the Fe NPs-Ni<sub>3</sub>S<sub>2</sub> NA/NF-10 at a constant current density of 80 mA cm<sup>-2</sup> for 30 h.

- 20 C. Z. Yuan, Z. T. Sun, Y. F. Jiang, Z. K. Yang, N. Jiang, Z. W. Zhao, U. Y. Qazi, W. H. Zhang and A. W. Xu, *Small*, 2017, **13**, 1604161.
- 21 Y. Yang, K. Zhang, H. Lin, X. Li, H. C. Chan, L. Yang and Q. Gao, *ACS Catal.*, 2017, **7**, 2357–2366.
- 22 J. T. Ren and Z. Y. Yuan, *ACS Sustainable Chem. Eng.*, 2017, **5**, 7203–7210.
- 23 J. Q. Yan, H. Wu, P. Li, H. Chen, R. B. Jiang and S. Z. Liu, *J. Mater. Chem. A*, 2017, **5**, 10173–10181.
- 24 N. Yang, C. Tang, K. Y. Wang, G. Du, A. M. Asiri and X. P. Sun, *Nano Res.*, 2016, **9**, 3346–3354.
- 25 X. Du, X. Zhang, Y. Li and M. Zhao, *Int. J. Hydrogen Energy*, 2018, **43**, 19955.
- 26 X. Du, Z. Yang, Y. Li, Y. Gong and M. Zhao, *J. Mater. Chem. A*, 2018, **6**, 6938–6946.
- 27 L. Zeng, K. Sun, Z. Yang, S. Xie, Y. Chen, Z. Liu and C. Liu, *J. Mater. Chem. A*, 2018, **6**, 4485–4493.
- 28 G. Zhang, Y. Feng, W. Lu, D. He, C. Wang, Y. Li and F. Cao, *ACS Catal.*, 2018, **8**, 5431–5441.
- 29 J. Diao, Y. Qiu, S. Liu, W. Wang, K. Chen, H. Li, W. Yuan, Y. Qu and X. Guo, *Adv. Mater.*, 2020, **32**, 1905679.
- 30 Y. Zhang, Y. Liu, M. Ma, X. Ren, Z. Liu, G. Du, A. M. Asiri and X. Sun, *Chem. Commun.*, 2017, **53**, 11048–11051.
- 31 T. Liu, X. Ma, D. Liu, S. Hao, G. Du, Y. Ma, A. M. Asiri, X. Sun and L. Chen, *ACS Catal.*, 2017, **7**, 98–102.
- 32 X. Xiong, C. You, Z. Liu, A. M. Asiri and X. Sun, *ACS Sustainable Chem. Eng.*, 2018, **6**, 2883–2887.
- 33 T. Liu, D. Liu, F. Qu, D. Wang, L. Zhang, R. Ge, S. Hao, Y. Ma, G. Du, A. M. Asiri, L. Chen and X. Sun, *Adv. Energy Mater.*, 2017, **7**, 1750020.
- 34 R. Zhang, C. Tang, R. Kong, G. Du, A. M. Asiri, L. Chen and X. Sun, *Nanoscale*, 2017, **9**, 4793–4800.
- 35 P. Wang, Z. Pu, Y. Li, L. Wu, Z. Tu, M. Jiang, Z. Kou, I. S. Amiinu and S. Mu, *ACS Appl. Mater. Interfaces*, 2017, **9**, 26001–26007.
- 36 S. Lee, K. Banjac, M. Lingensfelder and X. Hu, *Angew. Chem., Int. Ed.*, 2019, **58**, 10295–11029.
- 37 D. Friebel, M. W. Louie, M. Bajdich, K. E. Sanwald, Y. Cai, A. M. Wise, M. J. Cheng, D. Sokaras, T. C. Weng, R. Alonso-Mori, R. C. Davis, J. R. Bargar, J. K. Norskov, A. Nilsson and A. T. Bell, *J. Am. Chem. Soc.*, 2015, **137**, 1305–1313.
- 38 J. Y. Chen, L. Dang, H. Liang, W. Bi, J. B. Gerken, S. Jin, E. E. Alp and S. S. Stahl, *J. Am. Chem. Soc.*, 2015, **137**, 15090–15093.
- 39 M. Gorlin, J. Ferreira de Araujo, H. Schmies, D. Bernsmeier, S. Dresch, M. Gliech, Z. Jusys, P. Chernev, R. Kraehnert, H. Dau and P. Strasser, *J. Am. Chem. Soc.*, 2017, **139**, 2070–2082.
- 40 M. Gorlin, P. Chernev, J. Ferreira de Araujo, T. Reier, S. Dresch, B. Paul, R. Krahnert, H. Dau and P. Strasser, *J. Am. Chem. Soc.*, 2016, **138**, 5603–5614.
- 41 S. Lee, L. Bai and X. Hu, *Angew. Chem., Int. Ed.*, 2020, **59**, 8072–8077.
- 42 T. Wang, C. Wang, Y. Jin, A. Sviripa, J. Liang, J. Han and G. Wu, *J. Mater. Chem. A*, 2017, **5**, 25378–25384.
- 43 J. Liu, Y. Ji, J. Nai, X. Niu, Y. Luo, L. Guo and S. Yang, *Energy Environ. Sci.*, 2018, **11**, 1736.
- 44 S. Peng, C. Wang, J. Xie and S. Sun, *J. Am. Chem. Soc.*, 2006, **128**, 10676–10677.
- 45 S. Sun, H. Zeng, D. B. Robinson, S. Raoux, P. M. Rice, A. X. Wang and G. Li, *J. Am. Chem. Soc.*, 2004, **126**, 273–279.
- 46 J. Yan, Z. Fan, W. Sun, G. Ning, T. Wei, Q. Zhang, R. Zhang, L. Zhi and F. Wei, *Adv. Funct. Mater.*, 2012, **22**, 2632–2641.
- 47 C. Wang, H. Yang, Y. Zhang and Q. Wang, *Angew. Chem., Int. Ed.*, 2019, **58**, 6099–6103.
- 48 C. G. Zhou, L. C. Yin, D. W. Wang, L. Li, S. Pei, I. R. Gentle, F. Li and H. M. Cheng, *ACS Nano*, 2013, **7**, 5367–5375.
- 49 S. Liu, T. Zhao, X. Tan, L. Guo, J. Wu, X. Kang, H. Wang, L. Sun and W. Chu, *Nano Energy*, 2019, **63**, 103894.
- 50 O. Diaz-Morales, D. Ferrus-Suspedra and M. T. Koper, *Chem. Sci.*, 2016, **7**, 2639–2645.
- 51 D. Friebel, M. W. Louie, M. Bajdich, K. E. Sanwald, Y. Cai, A. M. Wise, M.-J. Cheng, D. Sokaras, T.-C. Weng and R. Alonso-Mori, *J. Am. Chem. Soc.*, 2015, **137**, 1305–1313.
- 52 S. Trasatti, *Electrochim. Acta*, 1984, **29**, 1503–1512.
- 53 J. Hu, S. Li, J. Chu, S. Niu, J. Wang, Y. Du and P. Xu, *ACS Catal.*, 2019, **9**, 10705–10711.
- 54 Y. Lu, Y. Deng, S. Lu, Y. Liu, J. Lang, X. Cao and H. Gu, *Nanoscale*, 2019, **11**, 21259–21265.
- 55 M. Liu, L. Kong, X. Wang, J. He and X. Bu, *Small*, 2019, **15**, 1903410.
- 56 J. Chen, F. Zheng, S. Zhang, A. C. Fisher, Y. Zhou, Z. Wang and S. Sun, *ACS Catal.*, 2018, **8**, 11342–11351.
- 57 J. Kibsgaard and T. F. Jaramillo, *Angew. Chem., Int. Ed.*, 2014, **53**, 14433–14437.
- 58 X. Du, Q. Wang, Y. Li and X. Zhang, *Dalton Trans.*, 2018, **47**, 10273.
- 59 X. Zhang, W. Sun, H. Du, R. M. Kong and F. Qu, *Inorg. Chem. Front.*, 2018, **5**, 344–347.
- 60 C. Tang, A. M. Asiri and X. Sun, *Chem. Commun.*, 2016, **52**, 4529–4532.